

Nikolopoulos, N., Strotos, G., Nikas, K-S., Theodorakakos, A., Gavaises, M., Marengo, M. & Cossali, G. E. (2010). Single droplet impacts onto deposited drops. Numerical analysis and comparison. *Atomization and Sprays*, 20(11), pp. 935-953. doi: 10.1615/AtomizSpr.v20.i11.20



**CITY UNIVERSITY
LONDON**

[City Research Online](#)

Original citation: Nikolopoulos, N., Strotos, G., Nikas, K-S., Theodorakakos, A., Gavaises, M., Marengo, M. & Cossali, G. E. (2010). Single droplet impacts onto deposited drops. Numerical analysis and comparison. *Atomization and Sprays*, 20(11), pp. 935-953. doi: 10.1615/AtomizSpr.v20.i11.20

Permanent City Research Online URL: <http://openaccess.city.ac.uk/13584/>

Copyright & reuse

City University London has developed City Research Online so that its users may access the research outputs of City University London's staff. Copyright © and Moral Rights for this paper are retained by the individual author(s) and/ or other copyright holders. All material in City Research Online is checked for eligibility for copyright before being made available in the live archive. URLs from City Research Online may be freely distributed and linked to from other web pages.

Versions of research

The version in City Research Online may differ from the final published version. Users are advised to check the Permanent City Research Online URL above for the status of the paper.

Enquiries

If you have any enquiries about any aspect of City Research Online, or if you wish to make contact with the author(s) of this paper, please email the team at publications@city.ac.uk.

Single droplet impacts onto deposited drops. Numerical analysis and comparison

by

N. Nikolopoulos^{1,*}, G. Strotos¹, K.-S. Nikas¹, A. Theodorakakos², M. Gavaises³, M. Marengo⁴, G.E. Cossali⁴

¹ Technological Education Institute of Piraeus, Mechanical Engineering Department, Fluid Mechanics Laboratory, 250 Thivon & P. Ralli str., Aegaleo, 12244, Greece

² Fluid Research Co. 49 Laskareos Str, 11472, Athens, Greece

³ City University London, School of Engineering and Mathematical Sciences

Northampton Square, EC1V 0HB, London, UK

⁴ Dept. of Industrial Engineering, University of Bergamo, viale Marconi 5, 24044 Dalmine, Italy

* Correspondence author email: niknik@fluid.mech.ntua.gr

Abstract. The impact of a spherical water droplet onto a stationary sessile droplet lying onto a solid wall is studied numerically using the VOF methodology. The governing Navier-Stokes equations are solved both for the gas and liquid phase coupled with an additional equation for the transport of the liquid interface. An unstructured numerical grid is used along with an adaptive local grid refinement technique, which enhances the accuracy of the numerical results along the liquid-gas interface and decreases the computational cost. The stationary sessile droplet has been created from the prior impact of one or two water droplets falling onto the solid wall, while two solid walls have been studied; an aluminium substrate and a glass substrate. The material of the wall plays an important role since it has an impact on the droplet's wetting behavior. The

numerical model is validated against corresponding experimental data presented in the first part of the present work [1], showing a good agreement. Furthermore, the numerical investigation sheds light into the governing physics of the phenomenon.

Keywords: VOF, droplet, impact onto a sessile droplet

1 Introduction

The sequential impact of droplets onto solid or liquid surfaces is an interesting phenomenon which can be found in many engineering applications such as metallurgical industry, surface cooling, fire suppression, electronic circuits, inkjet printing etc. The fluid flow associated with impinging droplets is quite complicated and depends on many parameters such as the nature of the impinging surface (solid or liquid), the solid surface's roughness and wettability, the thickness of the liquid film (h), the liquid and gas properties, the temperature of the surface, the angle of incidence, the impact velocity U_0 and the droplet diameter D_0 . The investigation of the phenomenon requires the examination of the most significant dimensionless numbers, such as the Weber number (We), the Reynolds number (Re) and the Froude number (Fr), defined as:

$$We = \frac{\rho_1 U_0^2 D_0}{\sigma}, \quad Re = \frac{\rho_1 U_0 D_0}{\mu_1}, \quad Fr = \frac{U_0^2}{g D_0} \quad (1)$$

Other dimensionless numbers often used, relevant to the aforementioned, are the Ohnesorge (Oh) and the Bond (Bo) number, defined as:

$$Oh = \frac{We^{1/2}}{Re} = \frac{\mu_1}{\sqrt{\rho_1 \sigma D_0}}, \quad Bo = \frac{We}{Fr} = \frac{\rho_1 g D_0^2}{\sigma} \quad (2)$$

The present investigation examines the impact of a droplet onto a stationary droplet. The phenomenon is expected to be a combination of the phenomena observed during droplet impact either onto a solid wall or onto a shallow film. A brief review of the phenomena observed during droplet impact onto solid and liquid surfaces is presented (a comprehensive description of these

phenomena can be found in Rein 1993 [2]), along with some representative numerical works related with these phenomena. Then the interest is turned to the sequential impact of droplets, which is the object of study in the present work.

The impact of a droplet onto a solid wall can be followed by either its sticking on the surface, its bouncing, its spreading or its splashing. The phenomenon is mainly governed by the We and Re numbers (calculated with the component velocity of the droplet along the axis of gravity just before its impact) as also by the liquid-solid wetting contact angle. The increase of We number results in the successive existence of the aforementioned regimes. When the droplet touches the solid surface a liquid torus called lamella is formed. Lamella expands radially with an initial velocity much greater than the impact velocity. Lamella's kinetic energy is gradually lost due to viscous and surface tension forces and droplet's expansion reaches a maximum. Then, due to surface tension forces the lamella contracts towards the axis of symmetry, while a second expansion wave may take place. Sometimes the contraction phase may be so intense, that a portion of the liquid mass is separated from the edge of the contracting liquid known as partial rebound. It has also been observed that at the contraction phase a bubble may be entrapped inside the liquid mass. For high We numbers, the lamella during its expansion phase may disintegrate into secondary droplets (splashing). Another important parameter, which should be addressed, is the wetting behavior of the droplet with the solid surface. A motionless droplet on a solid surface (sessile droplet) forms a contact angle at the triple point, where the three discrete phases are in equilibrium, called static contact angle. On the other hand, the moving front of the lamella at the expansion phase forms a greater angle called advancing contact angle, while at the receding phase forms a smaller angle called the receding contact angle. These three contact angles (advancing, static and receding) play a major role in droplet impacts and may influence the abovementioned regimes. The assumption of any contact angle (static, advancing, dynamic) as a boundary condition of the simulation is a statement which is mathematically and physical incorrect, since the contact angle itself for non-stationary flows is the result of the fluid dynamics near the contact line, as for the dip coating simulation. Nevertheless, since the real effect of the surface wettability is important only at the end of the spreading it is considered here an acceptable hypothesis. Moreover since the paper is mainly describing drop-on-drop impact the contact angle effects are linked only to the displacement of the liquid bulk on the surface, where the hypothesis of slow fluid flow is valid as for a equilibrium advancing contact angle at the contact line.

On the other hand, the impact of droplets onto a liquid layer exhibits a different behavior, which is controlled by We and Fr numbers, as also by the thickness of the underlying film relative to droplet's diameter $\delta=h/D_o$, while the wetting contact angles doesn't play any role since the whole solid surface is covered by liquid. When $\delta<1$ the liquid film is assumed to be shallow, while for $\delta >1$ the liquid film is deep. In both cases, the impacting droplet creates a crown, which expands both radially and vertically and has a non-uniform thickness in time and space. Its upper expanding part is called rim and investigations are usually concentrated on the diameter of the rim, as also the height of the rim. Certain combinations of values of the abovementioned parameters can lead to crown fragmentation and secondary droplet jetting, or to crown deposition onto the liquid layer with a subsequent formation of surface waves in the liquid film. Generally, the impact of a droplet onto a liquid film can lead to floating, bouncing, coalescence and splashing, while the two later are the most common. In the case of coalescence, a small crater is formed, without the creation of secondary droplet, while it is usually followed by the creation of vortex rings which penetrate inside the liquid film. The regime known as splashing is characterized by great disturbance of the film structure. The crater, which is formed at the area of impact results in the rise of a liquid column. This column may break-up into secondary droplets, while at latter stages the crater sides may join and enclose a gas bubble.

The crater dimensions increase with increasing We and Fr numbers. Simultaneously, in the interior of the film, intense recirculation zones are formed (vortex rings), whilst further increase of We number may lead to a vertical rise of liquid mass at the point of impact. For high We numbers, the liquid column can break-up into smaller droplets.

In the case of a shallow film, different regimes are identified since the thickness of the liquid layer is small and cannot absorb the energy of the impacting droplet. In the majority of these cases vortex rings are not observed, while the present investigation is more relevant with that case than the previous one. Due to the importance of the abovementioned phenomena a large number of experimental and numerical studies have been performed in order to shed light to the governing physics. In the first part of the present work, the most representative experimental works were presented. Here, the interest is turned to the numerical ones. A lot of numerical approaches have been adopted so as to simulate the impact of a droplet onto a solid surface or a liquid film. The spreading of a droplet on a solid surface was quantified analytically assuming energy conservation in [3], [4], [5], while a detailed simulation of the phenomenon has been treated with the solution of the Navier-Stokes equations. Such methodologies are the Marker and

Cell (MAC) by [6], [7], the Lagrangian formulation in a body fitted grid by [8], [9], [10], [11], [12], [13], the Immersed Boundary Method (IBM) by [14], [15], the Level-Set (LS) methodology by [16], the VOF methodology initially proposed by [17] and used in the works of [18], [19], [20], [21], [22], [23], [24]. In the aforementioned works the limiting conditions that separate the different regimes of the phenomenon were identified in the case of a droplet impact onto a wall and the maximum droplet spreading is estimated. A lot of these works include also the solution of the energy equation as in [23], [24] in which the levitation of a droplet over the substrate above a high temperature surface was predicted. Furthermore, the contra phenomenon i.e. the solidification of a droplet was also modeled in [19], [20], [21].

On the other hand, the impact of a droplet onto a liquid film has been addressed in many works.

Oguz & Prosperetti (1989) [25] used the Boundary Integral Method for an inviscid liquid to study the impact of a droplet on a liquid film and they were the first that identified the existence of bubble rings entrapping inside the liquid. Later, Oguz & Prosperetti (1990) [26] extended their numerical model and they defined the condition under which a primary bubble entrapment occurs.

Yarin & Weiss [1995] [27] developed an one-dimensional analytical model for the crown evolution, assuming a kinematic discontinuity in velocity and film thickness, while the crown breakup was attributed to instabilities of the liquid rim. It was estimated that the temporal evolution of the radius of the rim follows a power law with the power being equal to 0.5.

Weiss and Yarin (1999) [28] employed a boundary-integral method for the study of drop impact onto wet walls. They ignored viscosity as also the influence of the ambient gas. Their results for the rim radius were in good agreement with the power law of [27], while the mechanisms of bubble entrapment were also discussed. Trujillo and Lee (2001) [29] extended the model of Yarin and Weiss (1995) [27] by including the viscous losses, which was found to be of minor importance, except of the case of low Re number in which the thickness of the liquid film may influence crown propagation.

Roisman and Tropea (2002) [30] extended the analysis of Yarin and Weiss (1995) [27] by applying the laws of mass, momentum and energy conservation for the region of the base of the crown. They provided equation describing the temporal evolution of rim's radius and height and their results were in good agreement with experimental data for thin liquid films. Except of the

aforementioned analytical models, a detailed description of the phenomenon was performed solving the Navier-Stokes equations.

Reiber and Frohn (1999) [31] used the volume-of-fluid (VOF) methodology to investigate crown evolution in a three-dimensional geometry and taking into consideration the presence both of the gas phase as also of the liquid viscosity. Crown breakup owed to Rayleigh instabilities was numerically investigated by applying artificially random velocity disturbances to the initial velocity field.

Morton et al. (2000) [32] investigated the flow regimes resulting from the impact of a droplet onto a deep liquid film by using the VOF methodology but neglecting the presence of air. They identified the formation of vortex rings, bubble entrapment and the formation of vertical Rayleigh jets.

Josserand and Zaleski (2003) [33] performed VOF simulations and employed a potential flow model everywhere except for a small neck region of the developed crown. They showed that the rim radius follows a power law satisfying the analytical results of Yarin and Weiss [27]. Xie et al. (2004) [34] used the moving particle semi-implicit (MPS) method to study the impact of a liquid drop onto a thin liquid film. Their model was validated against experimental data, but this method proved to be inaccurate when the liquid film becomes thin and breaks up into small droplets. Mukherjee & Abraham (2007) [35] examined the crown behavior during the impingement of a drop onto a liquid layer in axisymmetric coordinates by using the lattice-Boltzmann method. They found that increasing the gas density and viscosity suppresses the growth rate of the rim radius and height and delays the crown breakup.

For the case of chain droplet impact little information exists in the recent literature. Fujimoto et al. (2001) [36] studied the collision of a droplet with a static hemispherical droplet on a solid both numerically and experimentally. They solved the Navier-Stokes equations in an axisymmetric geometry taking into consideration the contact angle hysteresis, but ignoring the gas phase presence. Consequently, they couldn't identify if any gas bubble were entrapped. Their results were in good agreement with the experimental data for the initial stages of impact on the static droplet and they explained that the crown formation is owed to the pressure gradient formed inside the static droplet. The same authors (Fujimoto et al. 2001b) [37] also investigated numerically the collision of two successive droplets with a substrate at room temperature and they

pointed out that if the time interval between the droplet collision is large, the crown becomes high and large.

In Fujimoto et al. (2002) [38], the effects of the frequency the two droplets colliding on the solid wall was examined experimentally for a governing Weber number being equal to around 50. Fujimoto et al. 2004) [39] extended their investigation, adding as a parameter the temperature of the solid surface. Under the condition of We number close to 100, the surface temperature was varying between 120 °C and 500 °C. This investigation was also an after step of the same work but for conditions of low We number, performed by Karl and Frohn (2000) [40].

Tong et al. (2007) [41] studied the successive collision of droplets using the VOF methodology in axisymmetric coordinates and they investigated the effect of droplet impact frequency. Their model was validated against the experimental data of Fujimoto et al. (2002) [38] showing good agreement. The entrapment of gas bubbles and bubble rings was predicted in their simulations.

Fujimoto et al. (2008) [42] studied experimentally the successive collision of 2 water droplets either onto a cold or a hot surface. They investigated the effects of surface temperature, We number and frequency of collision and found that increasing the surface temperature results in the disintegration of the crown, which cannot be easily identified because of its early disintegration.

The present investigation focuses into the physical mechanisms governing the phenomenon of impact of a droplet onto a sessile droplet. By this work our intention is to fill the gap between droplet impact onto a solid wall and onto a shallow film and to investigate numerically the effects of sessile droplet thickness, impact velocity and solid substrate wetting behavior.

The present investigation applies the VOF methodology, which has been also been used in the past by authors' group using the GFS code [43] in order to predict a number of different cases in 2 or 3 dimensions. The cases examined up to now are the impingement of a droplet onto a liquid film [44], [45], binary droplet collisions [46], [47], [48] and the interaction of a droplet with a heated wall coupled with evaporation [49], [50], [51], the evaporation of suspended single-component and multi-component droplets in a convective gas environment [52], [53]. In these works an adaptive local grid refinement technique was used [54] reducing the computational cost, without loss of any numerical accuracy.

2 Mathematical Model

The flow induced by the collision of a droplet onto a sessile droplet is considered in the present study as two-dimensional axisymmetric, incompressible and laminar. This assumption is verified at the initial and middle stages of impact, whilst at the latter stages characteristics with a three dimensional character are evident. The flow induced is mathematically expressed by the conjugate solution of the Navier-Stokes equations and the continuity equation along with a transport equation for the gas-liquid interface. Each phase (gas and liquid) is identified by the volume fraction α (ratio of liquid volume in a cell over the cell volume), following the Volume of Fluid Method (V.O.F) methodology by Hirt & Nichols [1981] [17]. The α -function is equal to 1 for a point of the computational domain inside the liquid phase, 0 inside the gas phase and lies between 0 and 1 in the gas-liquid interface.

The transport properties in a computational cell (density ρ and viscosity μ) are calculated using linear interpolation between the values of the two phases weighted with the volume fraction α :

$$\begin{aligned}\rho &= \alpha \rho_l + (1 - \alpha) \rho_g \\ \mu &= \alpha \mu_l + (1 - \alpha) \mu_g\end{aligned}\tag{3}$$

The transport equation for the volume fraction (ignoring evaporation and density change) is:

$$\frac{\partial \alpha}{\partial t} + \nabla \cdot (\alpha \vec{u}) = 0\tag{4}$$

where \vec{u} is the velocity vector. The momentum equations are solved for both the liquid and the gas phase and are written in the form:

$$\frac{\partial(\rho \vec{u})}{\partial t} + \nabla \cdot (\rho \vec{u} \otimes \vec{u} - \vec{T}) = \rho \vec{g} + \vec{f}_\sigma\tag{5}$$

where \vec{T} is the stress tensor and \vec{f}_σ is the volumetric force due to surface tension. The later is a function of the surface tension coefficient σ and the local curvature κ at the computational cell. This volumetric source term acts only at the interface region and it is calculated according to the methodology proposed by Brackbill et al [1992] [55].

$$\vec{f}_\sigma = \sigma \cdot \kappa \cdot (\nabla \mathbf{a}) \quad (6)$$

The discretization of the convection terms of the velocity components is based on a high resolution convection-diffusion differencing scheme (HR scheme) proposed by Jasak [1996] [56]. On the other hand, the discretization of equation (4) needs a special treatment in order to avoid numerical diffusion and smearing of the interface. Thus, the high-resolution differencing scheme CICSAM proposed by Ubbink & Issa [1999] [57] is used and the time derivative is discretized using the second-order Crank-Nicolson scheme, as also small Courant number approximately 0.2-0.3.

3 Grid and Boundary Conditions

The non-linear system of the flow equations is solved numerically on a two-dimensional axisymmetric unstructured grid, using a recently developed adaptive local grid refinement technique, (Theodorakakos & Bergeles [2004] [54]), which enhances the accuracy at the interface region and achieves low computational cost compared to the case of a uniform grid with the same resolution.

A base grid is used and the cells at the region of the interface are subdivided according to the levels of local grid refinement used, while the interface lies always in the densest grid region since the grid is reconstructed every 10 timesteps. For the cases examined here, a base grid consisting of 3600 cells and 5 levels of local grid refinement was used. This resulted in a resolution of $D_0/516$ at the interface region, which found sufficient for a grid independent solution to be achieved after numerical tests. The number of computational cells varied from 17000 to 24000 (depending on the interface shape) while a uniform grid with the same resolution would require 3.68 million cells.

The computational domain and the boundary conditions used are shown in Fig. 1a while in Fig. 1b a snapshot of the automatically refined grid is shown. The southern boundary is assumed to be a solid impermeable wall with no-slip conditions as also a special treatment for the

implementation of the liquid-solid contact angle is considered as in Ubbink (2007) [58]. The western boundary is the symmetry axis with a zero normal velocity, while northern and eastern boundaries are assumed to be an open boundary with zero first gradients for all variables, except for the pressure at the northern boundary which is assumed constant and equal to atmospheric.

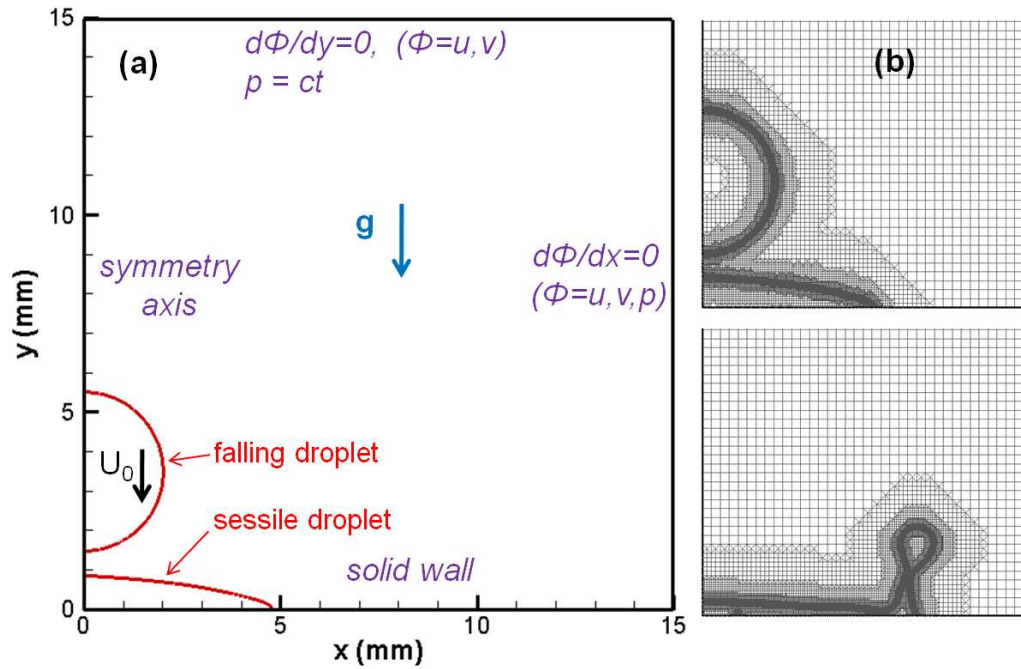


Fig. 1: Computational domain and boundary conditions (a). In (b) two frames showing the adaptive local refined grid are shown

4 Results and Discussion

4.1 Experimental data

Droplets with a diameter of $D_0=4.02\text{mm}$ are falling with velocities varying from 1.7 to 2.65m/s on a stationary sessile droplet, formed by the impact of the previous two and three droplets. Two materials of solid substrate were simulated (aluminum and glass), which resulted in different

wetting behavior of droplets; the liquid-solid advancing and receding contact angles for the aluminum substrate are 60° and 22° respectively, while for the glass substrate they are 10° and 6° respectively. Sessile droplet's dimensions are controlled by the impact of one or two droplets on the substrate, prior to the examined falling droplet; these cases are termed as «2 droplets» and «3 droplets» respectively. The experimental conditions for the cases examined in this paper, are summarized in Table 1.













	Case	Plate	$\theta_{adv}-\theta_{rec}$	h/D_0	U_0	We	Fr_h	Re
2 droplets	A2 	Al	$60^\circ-22^\circ$	0.215	1.70	160.9	340.5	6816.2
	B2 	Al	$60^\circ-22^\circ$	0.230	2.50	348.0	688.4	10023.8
	C2 	Al	$60^\circ-22^\circ$	0.234	2.60	376.4	731.8	10424.7
	D2 	Glass	$10^\circ-6^\circ$	0.130	2.20	269.5	943.1	8820.9
	E2 	Glass	$10^\circ-6^\circ$	0.146	2.40	320.8	999.4	9622.8
	F2 	Glass	$10^\circ-6^\circ$	0.120	2.65	391.1	1482.5	10625.2
3 droplets	A3 	Al	$60^\circ-22^\circ$	0.329	1.70	160.9	222.5	6816.2
	B3 	Al	$60^\circ-22^\circ$	0.277	2.50	348.0	571.6	10023.8
	C3 	Al	$60^\circ-22^\circ$	0.266	2.60	376.4	643.8	10424.7
	D3 	Glass	$10^\circ-6^\circ$	0.140	2.20	269.5	875.8	8820.9
	E3 	Glass	$10^\circ-6^\circ$	0.180	2.40	320.8	810.6	9622.8
	F3 	Glass	$10^\circ-6^\circ$	0.162	2.65	391.1	1098.1	10625.2

Table 1: Properties of the cases examined.

The measured quantities investigated in this work, are the crown rim radius R_{LR} , the base radius of the lamella R_{LB} and the rim height H . These magnitudes as also the initial thickness of the sessile droplet are shown in Fig. 2. An important parameter is the dimensionless droplet thickness, non-dimensionalised with the droplet diameter:

$$\delta = \frac{h}{D_0} \quad (7)$$

The numerical predictions for the aforementioned magnitudes will be presented in sections 4.2, 4.3 and 4.4 respectively. The time in the graphs presented will be non-dimensionalised as:

$$\tau = t \cdot \frac{U_0}{D_0} \quad (8)$$

Other important magnitudes like the number of secondary droplets formed will not be discussed since the axisymmetric approach adopted in the present investigation does not allow the exact representation of such phenomena.

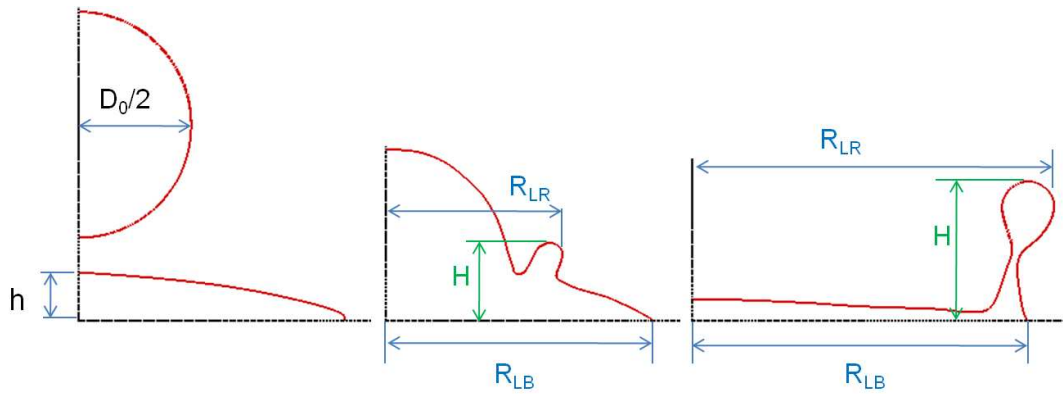


Fig. 2: Problem geometry and definition of the measured magnitudes.

4.2 Crown's radius

The results obtained from the numerical simulation of the examined cases for the temporal evolution of crown's dimensionless radius are presented in Fig. 3 for the cases of 2 droplets and in Fig. 4 for the cases of 3 droplets. In these figures the left one (a) refers to the aluminium substrate and the right one (b) to the glass substrate.

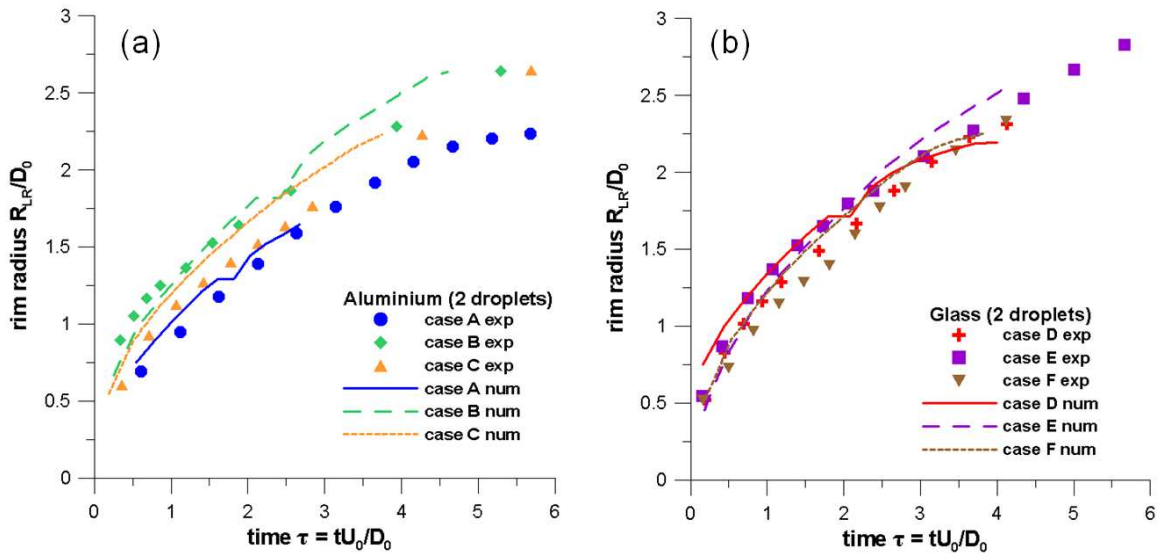


Fig. 3: Temporal evolution of rim's radius for impact on aluminium (a) and glass (b) substrate for the case of 2 droplets.

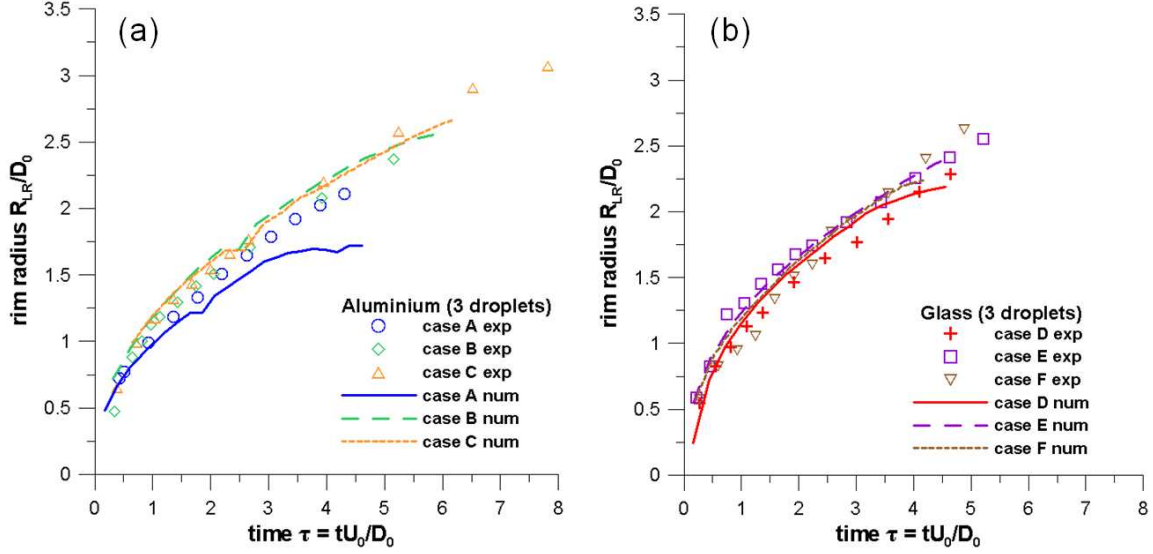


Fig. 4: Temporal evolution of rim's radius for impact on aluminium (a) and glass (b) substrate for the case of 3 droplets.

As it can be seen, the numerical predictions for the temporal evolution of crown diameter are in a good agreement with the corresponding experimental data and the deviations from the experimental data observed at later stages of the phenomenon, are attributed to the three-dimensional phenomena which become important and cannot be represented with validity by the present axisymmetric simulation.

4.3 Base radius

The results obtained from the numerical simulation of the examined cases as far as the temporal evolution of lamella's base dimensionless radius is concerned, are presented in Fig. 5 for the cases of 2 droplets and in Fig. 6 for the cases of 3 droplets.

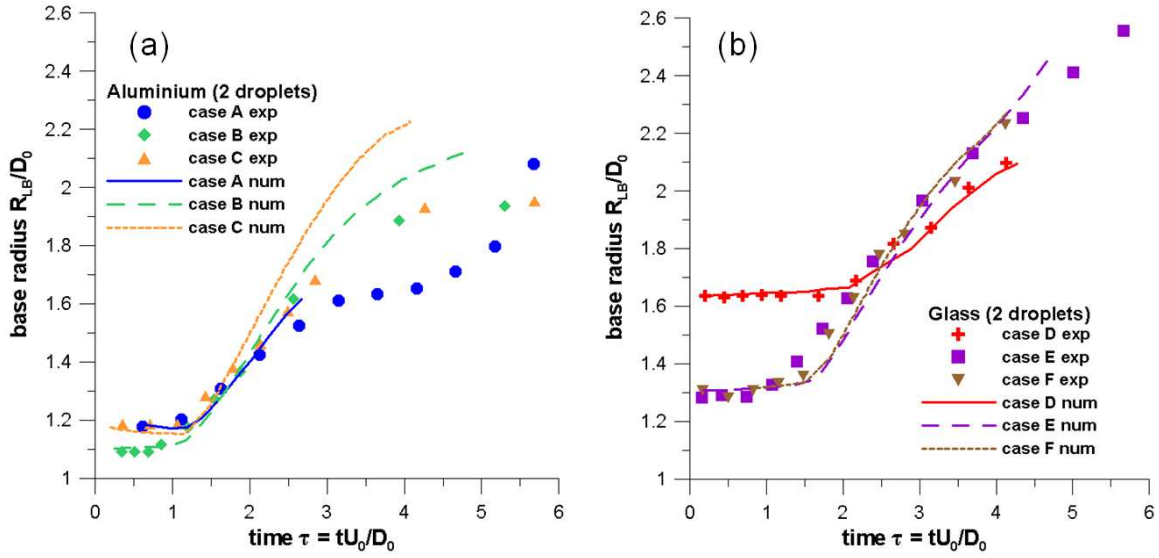


Fig. 5: Temporal evolution of base radius for impact on aluminium (a) and glass (b) substrate for the case of 2 droplets.

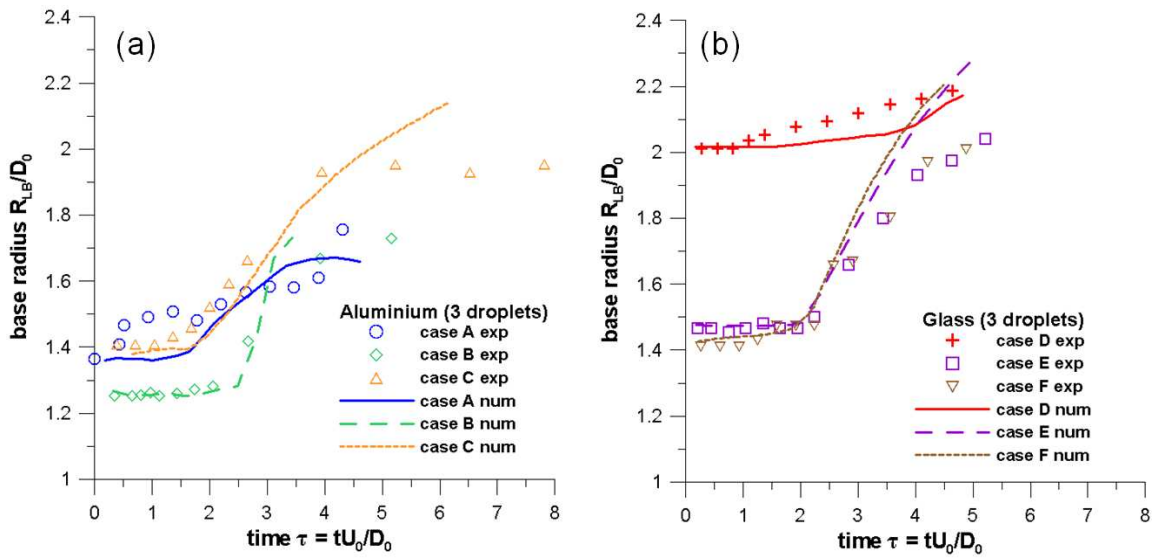


Fig. 6: Temporal evolution of base radius for impact on aluminium (a) and glass (b) substrate for the case of 3 droplets.

The results for the base radius are characterized by uncertainties in the experimental measurements. The predictions are in a good agreement with the corresponding experimental data, at the initial and middle stages of impact. At latter stages discrepancies between experimental data and numerical results are owed to the three dimensional character of the phenomenon, which cannot be represented with validity by the present axisymmetric formulation of the physical problem. The base radius is almost constant until around to $\tau=2$ and later the motion of the rim pushes the deposited lamella on the wall to move. That is the reason why there is a time delay for the base radius to increase. At later stages, which are not presented here, the deposited lamella on the wall recedes and finally reaches a stable form.

4.4 Crown's height

The results obtained from the numerical simulation of the examined cases for the temporal evolution of the non-dimensional crown's height are presented in Fig. 7 for the cases of 2 droplets and in Fig. 8 for the cases of 3 droplets. The height of the crown increases with time reaches a maximum and then decreases, under the effect of gravity. The three dimensional character of the deposited lamella and the large fingers, which are inducing on its top rim cannot be represented by the present numerical approach owed to its axisymmetric form.

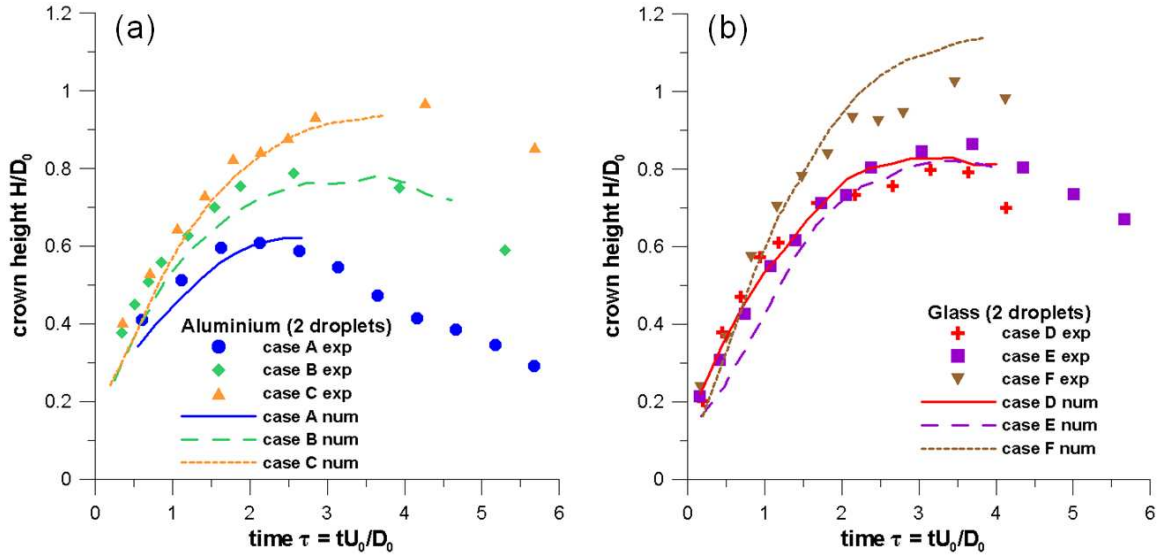


Fig. 7: Temporal evolution of crown's height for impact on aluminium (a) and glass (b) substrate for the case of 2 droplets.

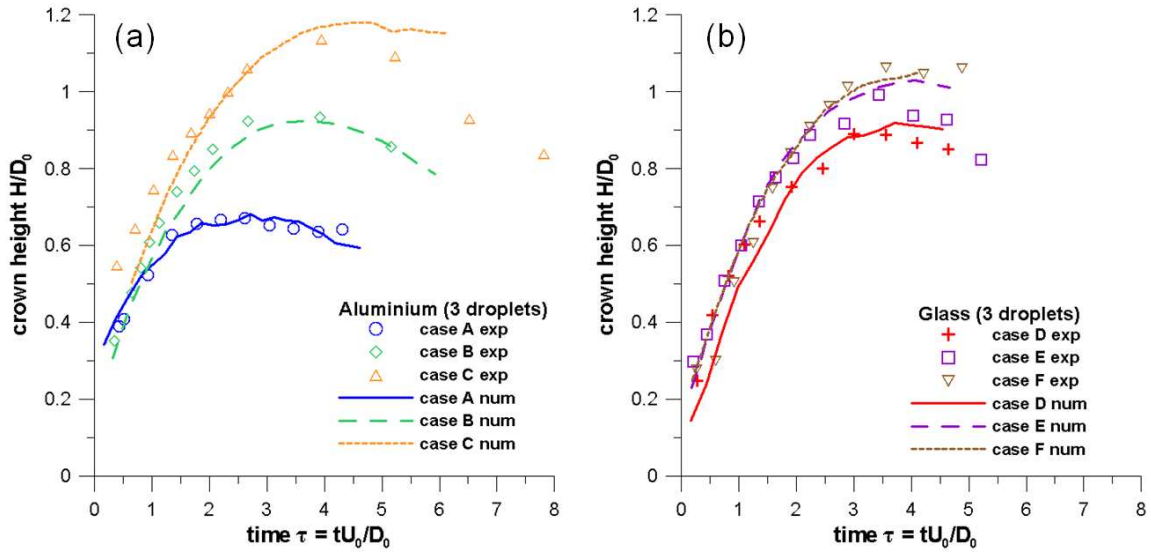


Fig. 8: Temporal evolution of crown's height for impact on aluminium (a) and glass (b) substrate for the case of 3 droplets.

4.5 Flow field regimes

In this section, selected frames showing the temporal evolution of droplet shape, dimensionless pressure and dimensionless velocity are presented for cases A2, C2 and F2 in Fig. 9, Fig. 10 and Fig. 11 respectively. Cases A2 and C2 have almost the same boundary conditions (2 droplets and aluminium surface) but different We numbers ($We=161$ and $We=376$ respectively), while cases C2 and F2 have similar We numbers but different boundary conditions regarding the shape of the sessile droplet. In these frames details of the flow field are also presented in enlarged pictures. The dimensionless pressure is presented in the left part of the pictures, while the dimensionless velocity magnitude is presented in the right part of the figures. These magnitudes are defined as:

$$p^* = \frac{p - p_\infty}{\frac{1}{2}\rho_1 U_0^2}, \quad U^* = \frac{|\vec{u}|}{U_0} \quad (9)$$

For reasons of distinctness, a narrow range of values for pressure and velocity is presented despite the fact that at the initial stages of impact large values are observed for these magnitudes. Furthermore, the gas-liquid interface presented, corresponds to a VOF value equal to 0.5.

For all cases, an advancing crown is created from the early stages of impact (Fig. 9 $\tau=0.613$, Fig. 10 $\tau=0.317$, Fig. 11 $\tau=0.165$) originating from the peripheral points of the junction of the falling droplet with the sessile droplet. The crown moves radially outwards and vertically upwards and at its edge a thicker rim is formed (Fig. 10 $\tau=1.092$). Its motion pulls the lower liquid mass to rise and the base of the sessile droplet increases.

Following the impact of the droplet on the film, liquid from the film is transferred to the lamella liquid sheet. In particular, in the crater the shallow film becomes even thinner and surface waves develop, as also reported by Weiss and Yarin (1999) [28]. For case A2 at time $\tau=4.92$ the minimum film height found at the crown's base, within the crater is equal to 3.4% of the initial droplet diameter, for case C2 at time $\tau=7.62$ is approximately 2.5% of the initial droplet diameter and finally for case F2 at time $\tau=7.41$ is approximately 1.7% of the initial droplet diameter. At the initial stages of impact ($\tau \approx 0$) the dimensionless pressure locally at the point of impact reaches a value of 6-7 and it is proved that the same value is observed for all cases, irrespective of impact velocity. This reveals the dimensionless character of the phenomenon as far as We number and wettability effects for the initial stages of the evolution of the phenomenon are concerned, at least

for the range of parameters investigated in this paper. Later, within a short time interval of approximately $\tau=0.1-0.6$ the maximum pressure is approximately equal to 1.8-2.5 and its distribution in space is forming an oblique pressure gradient pointing from the axis of symmetry towards the rim of the crown (Fig. 9 $\tau=0.613-1.120$, Fig. 10 $\tau=0.317-1.092$, Fig. 11 $\tau=0.165-0.823$). This pressure gradient is responsible for the formation of the crown, since it pushes liquid mass in the diagonal direction, while the shear stress from the recirculating gas phase at this region, enhances the development of the crown. At subsequent times the pressure inside the liquid is further decreasing and exhibits a quite uniform distribution in space

The velocity at the initial stages of impact exhibits large values in the order of 5-8 times the impact velocity, while the pick values are observed at the gas phase near the point at which the falling droplet touches the sessile droplet. Generally, the velocities found inside the liquid phase are small, whilst relatively increased velocities ($\sim 0.8-1.0U_0$) are observed at the rim. No recirculating regions are observed inside the liquid, since there is no receding phase, in contrast to the gas phase, in which large vortices attached to the moving droplet are observed; these vortices are shown in the enlarged regions of Fig. 9, Fig. 10 and Fig. 11.

Of exceptionate interest is the fact that the entrapment of gas bubbles is predicted in all frames of the cases examined as a result of the pressure built up at the point of impact. Furthermore, in case F2, except of the gas bubble entrapped at the axis of symmetry, a bubble ring is also observed (Fig. 11 $\tau=0.165-0.494$) which is expected to break into small peripheral bubbles; the latter has been identified numerically in Oguz & Prosperetti (1989) [25] as also by Tong et al. (2007) [41] and its existence has been experimentally verified by Thoroddsen et al. (2003) [59]. The volume of the gas inside the liquid mass is approximately in the range from 1.8 to $3.8 \cdot 10^{-5}V_0$

In all cases examined three-dimensional effects are observed at later times. On the other hand, as seen in cases C2 and F2 controlled by high We number ($We=376$ and $We=391$ respectively), a liquid ring is cut off from the rim at the early stages of impact. In fact, this ring breaks-up into a number of small secondary droplets, but the axisymmetric approach adopted here can be still considered reliable, since their size is very small. Furthermore, the liquid torus formed at subsequent times, is also separated from the liquid mass (Fig. 10, $\tau=3.87$). Regarding the main characteristics of the induced flow field, during the life time of the crown a kidney type vortex ring is attached to its evolutionary rim on its top, as it can be seen by Fig. 10, $\tau=0.704$, Fig. 11, $\tau=0.165$.

Wu (2003) [60] derived an approximate torus Weber number $We_{tor,cr}$, above which an expanding torus disintegrates into secondary droplets, under the assumption of Rayleigh instability. The Weber number used (We_{tor}) is defined using as reference length the diameter of a sphere having the volume with the torus and an equivalent velocity of a sphere having the same energy (kinetic and surface) with the torus, i.e. $We_{tor} = \rho_{liq} U_{equiv}^2 D_{equiv} / \sigma$. For the definition of these magnitudes he used the diameter of the torus d_c and the diameter of the cross section of the torus d_{se} ; these magnitudes are clearly defined in [60]. According to Wu (2003) [60] the approximate critical $We_{tor,cr}$ for the breakup of an expanding torus is given by $We_{tor,cr} = 22.48 \ln^{2/3}(1/r_a)$, where r_a is the relative initial perturbation. It is assumed that the magnitude of the initial perturbations on the crown's rim is the same with that of the induced surface waves on the film surface, implying that is r_a of the order of $O[10^{-2}]$. For this wave amplitude a Weber number of the order of 60 is calculated. This theory is applied in the present cases assuming that the crown rim is a torus, at the time of its detachment and calculating the average We_{tor} number at different times.

For case A2 the value of We_{tor} for all times of the advancing phase of the crown is below 60, equal to around 10-20, thus suggesting that according to this theory no disintegration into a number of secondary droplets should be expected. This is confirmed by both the present numerical results and the corresponding experimental data. In contrast, for cases C2 and F2, according to the values of Table 2 calculated by the present numerical results, during the initial stages of impact ($\tau=0.252$, $\tau=0.510$ and $\tau=0.704$ for case C2 and $\tau=0.494$ for case F2) disintegration is expected, which is confirmed by the corresponding experimental data. Nevertheless, owed to the adopted axisymmetric approach the creation of secondary droplets cannot be reproduced. Table 2 presents the numerical results for these cases in detail.

Case	τ	U_{tor}	$d_c \cdot 10^3$	$d_{\text{se}} \cdot 10^3$	$d_{\text{equiv}} \cdot 10^3$	We_{tor}
C2	0.252	4.25	5.214	0.105	0.647	165.63
	0.510	2.63	7.111	0.148	0.903	90.12
	0.704	2.23	8.199	0.229	1.265	89.09
	3.741	0.52	17.855	0.699	3.453	13.55
F2	0.494	2.84	7.106	0.170	0.989	113.19

Table 2: Variables concerning the torus rim evolution for cases C2 and F2.

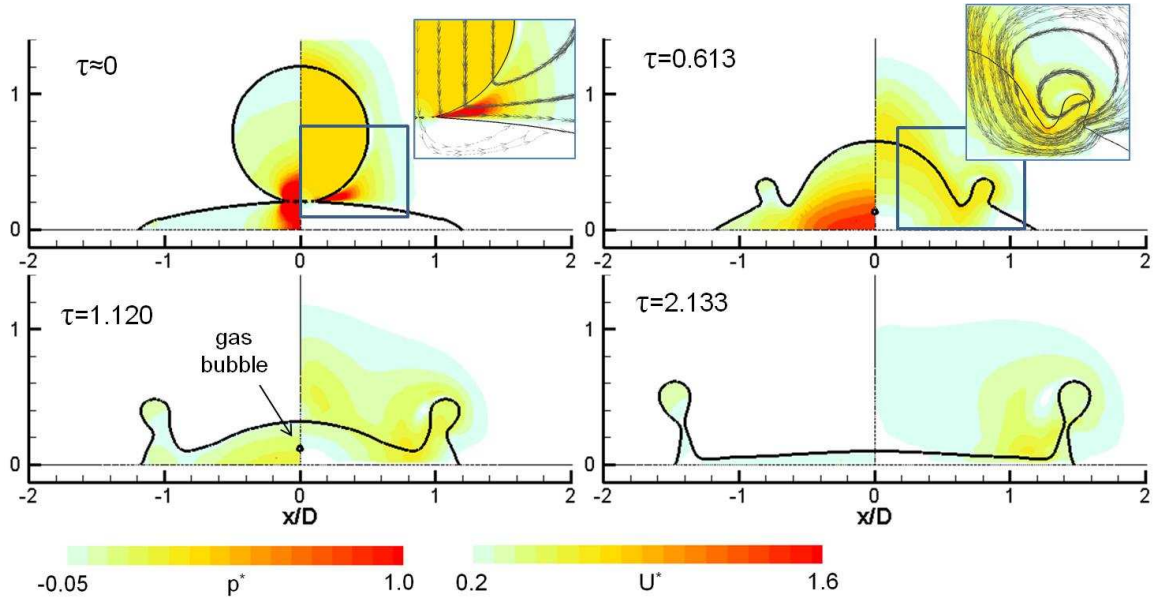


Fig. 9: Selected frames of case A2 ($We=161$, $Fr_h=340$) showing the gas-liquid interface, the dimensionless pressure distribution (left hand side) and the dimensionless velocity distribution (right hand side). In the enlarged regions, representative streamlines are shown.

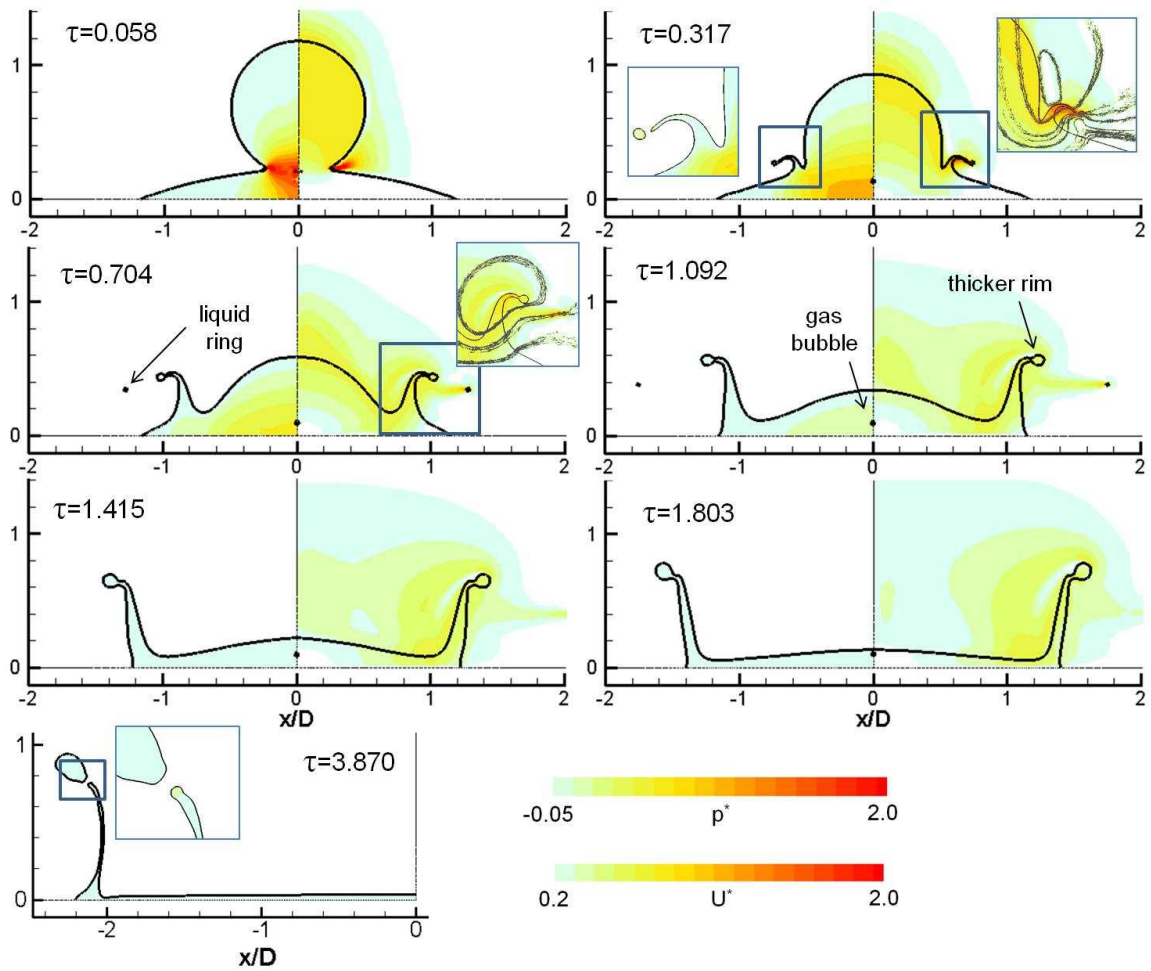


Fig. 10: Selected frames of case C2 ($We=376$, $Fr_h=732$) showing the gas-liquid interface, the dimensionless pressure distribution (left hand side) and the dimensionless velocity distribution (right hand side). In the enlarged regions, representative streamlines are shown.

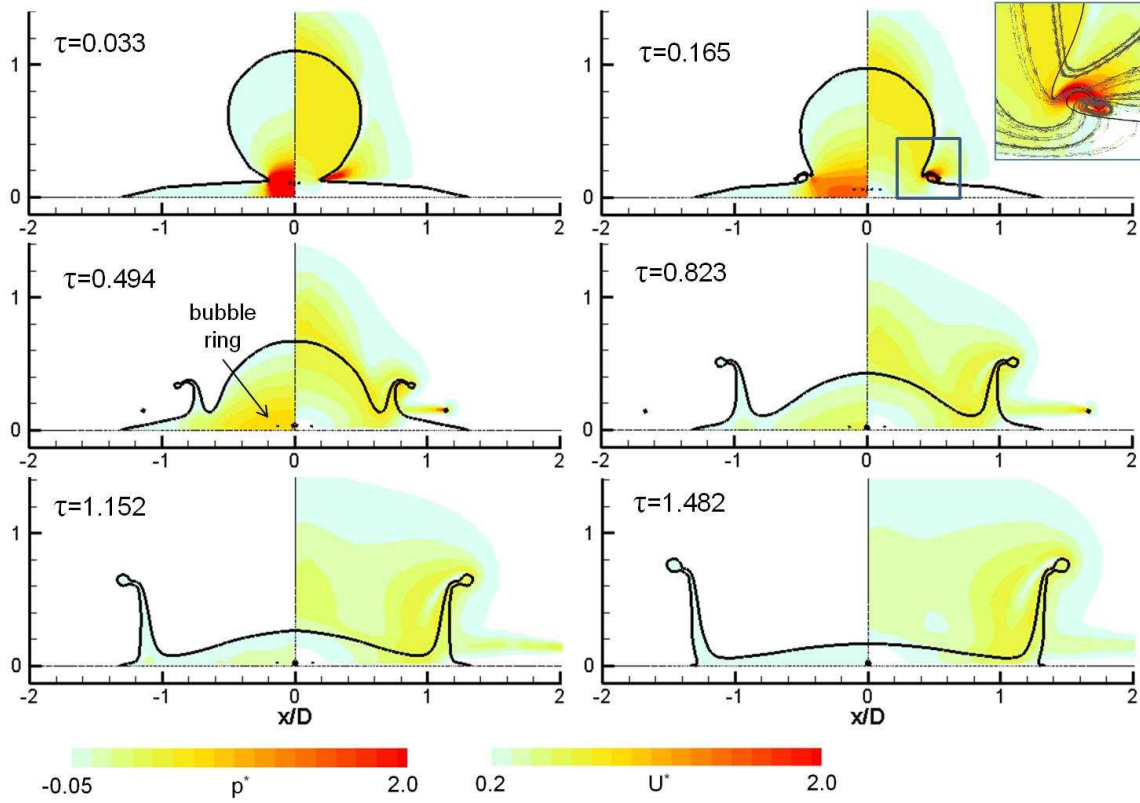


Fig. 11: Selected frames of case F2 ($We=391$, $Fr_h=1483$) showing the gas-liquid interface, the dimensionless pressure distribution (left hand side) and the dimensionless velocity distribution (right hand side). In the enlarged regions, representative streamlines are shown.

Another point which may be of interest is the estimation of the boundary layer thickness. The boundary layer is in fact linked to the viscous dissipation, which in turn is playing an important role for the spreading and the splashing regimes. There is a region of about $300\mu\text{m}$ (about 30% of the radial length) where the velocity has the strongest gradient and, in fact, the neck of the ejecting lamella has a thickness of about $300\mu\text{m}$ (**Fig. 12**).

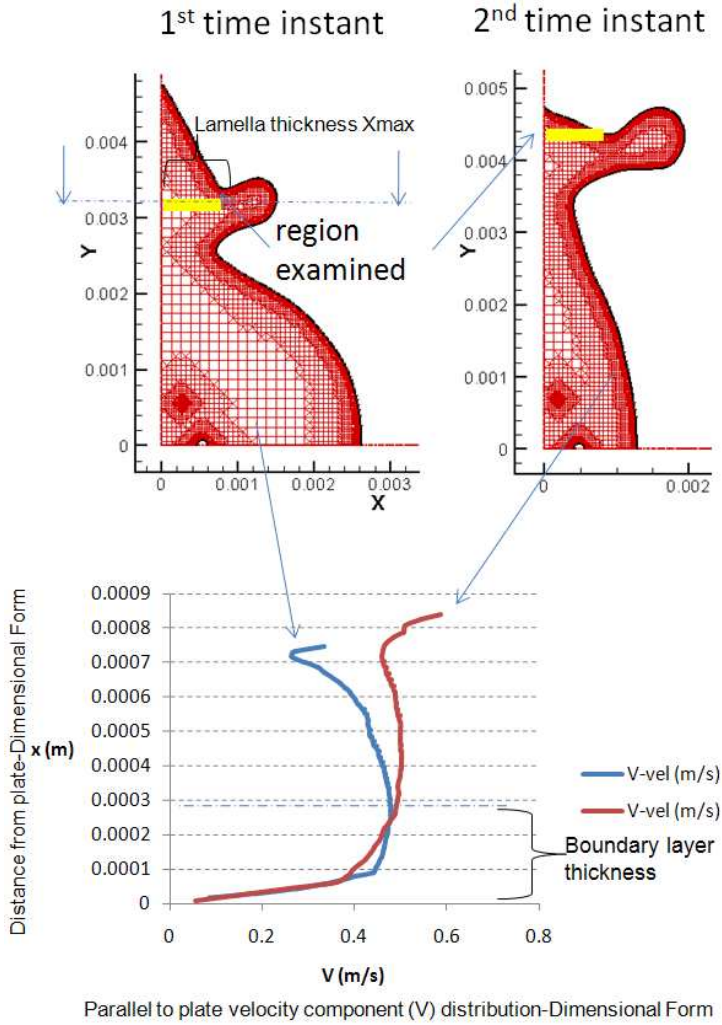


Fig. 12: The maximum thickness of the boundary layer near the lamella ejection

4.6 Ejecta sheet

In this section the interest is turned to the early stages of impact in which an ejecta sheet is formed. Ejecta sheet is the liquid structure formed in the vicinity of the impact of a droplet onto a liquid film during the early stages of impact, which at later time forms the crown. Generally, ejecta sheets propagate radially (but may also bend) and are characterized by high velocities which rapidly decrease under the action of surface tension and viscous forces. The ejecta sheet is

observed in all cases examined and it is presented in Fig. 13 for the cases D2, E2 and F2. These are characterized by intermediate and high We numbers ($We=269, 321$ and 391 respectively). For case D2 ($We=269$) the ejecta sheet expands radially and finally forms the crown (as discussed in section 4.5 but not shown in Fig. 13). The case E2 has a higher We number equal to 321 and during the expansion of the ejecta sheet, it bends (Fig. 13, E2 $\tau=0.059$) and connects with the underlying liquid forming a toroidal bubble (Fig. 13, E2 $\tau=0.119$). This bending of the ejecta sheet has been observed experimentally by Thoroddsen (2002) [61]. Finally, in case F2 with an even higher We number of 391 , the ejecta sheet bends as in the previous case, but due to the high inertia of the impact, the leading edge of the ejecta sheet is separated and forms a liquid ring which is expected to break into several secondary droplets.

Thoroddsen 2002 [61] performed experiments with droplets falling onto a relatively thick liquid film ($\delta=1.71$) at a constant We number of 2350 and Re number in a range from 350 up to 29000 by varying the liquid viscosity. The droplet diameter was also constant ($D=6\text{mm}$) and despite the fact that he mentions that for a pure water droplet no ejecta sheet was observed, here an ejecta sheet is predicted even for much smaller We numbers. Nevertheless, the present cases are different from the ones examined by [61] since the droplets examined here are smaller ($D=4.024\text{mm}$) and the maximum droplet thickness was less than 0.329 . The later is believed to have a more severe impact, since the solid wall is closer to the vicinity of interest and the induced momentum wave after the impact of the droplet is reflected from the wall and promote the formation of the ejecta sheet.

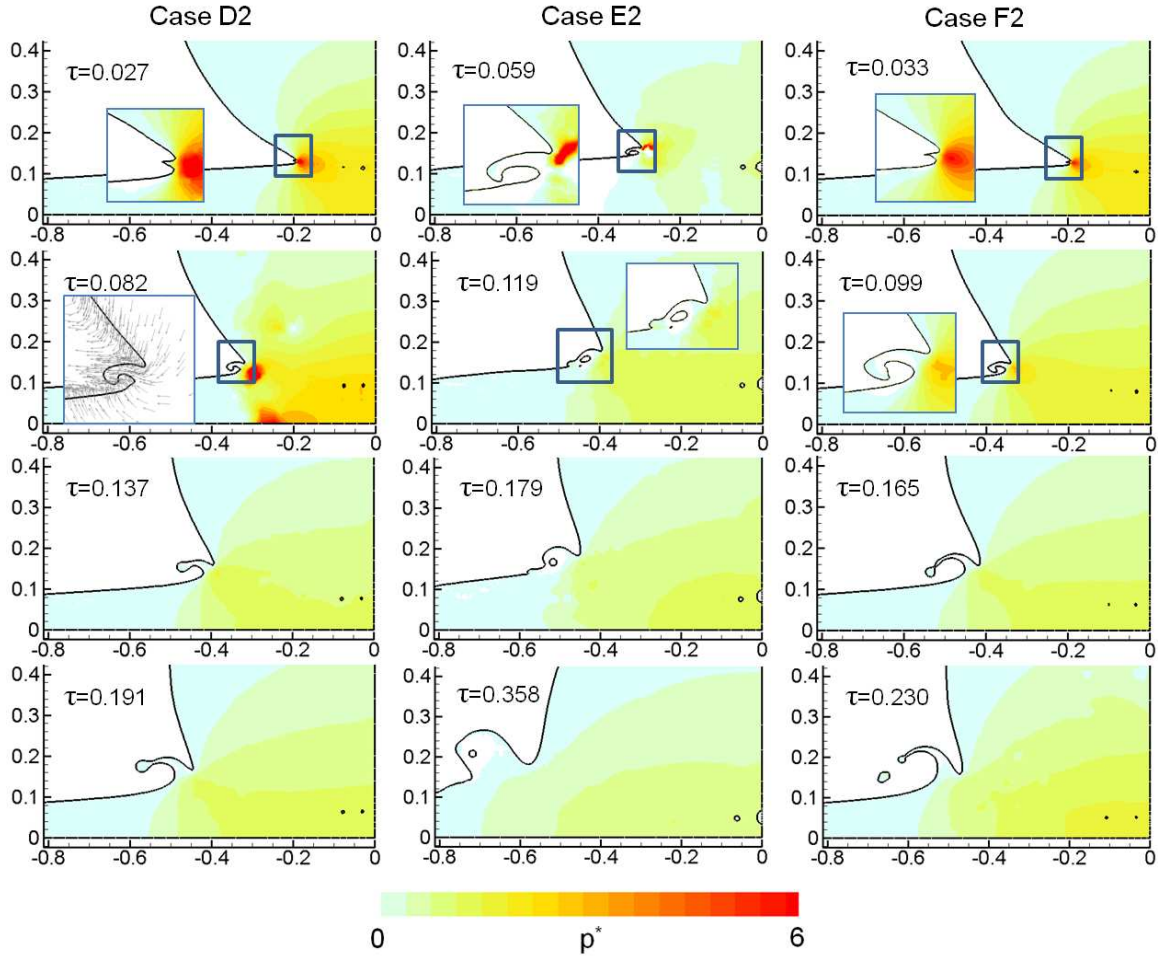


Fig. 13: Selected frames of case D2, E2 and F2 ($We=269, 321$ and 391) showing the formation of the ejecta sheet. The dimensionless pressure distribution is also presented and the dimensions are non-dimensionalised with the droplet diameter.

As referred by Thoroddsen 2002 [61] the ejecta sheet propagates at the initial stages with a high velocity, even 10 times the impact velocity. The measured velocities of the ejecta sheet non-dimensionalised with the impact velocity are plotted versus the dimensionless time in Fig. 14a for all cases examined during the initial stages of impact. The experimental data of Thoroddsen (2002) [61] and the numerical predictions of Nikolopoulos et al. (2005) [44] are also presented. These data refer to the collision of a high viscous liquid droplet ($\mu=29\text{cP}$) falling onto a relatively thick film ($\delta=1.71$). Despite the fact that the present cases refer to a droplet impact onto a sessile one collision, it is proved that the ejecta sheet velocity evolves with the same fashion.

As discussed in the first part of the present work, the crown's radius can be theoretically estimated according to Yarin & Weiss [1995] [27] as:

$$\left(\frac{R_{LR}}{D_0} \right)_{\text{film,th}} = C_{\text{film,th}} (\tau - \tau_0)^n, \quad C_{\text{film,th}} = \left(\frac{2}{3\delta} \right)^{0.25}, \quad n = 0.5 \quad (10)$$

Equation (10) is proved to give rational results. So, a rough estimation of the ejecta sheet velocity could be obtained by differencing over time equation (10):

$$\frac{U_{\text{sheet}}}{U_0} = n C_{\text{film,th}} (\tau - \tau_0)^{n-1} \rightarrow \frac{U_{\text{sheet}}/U_0}{n C_{\text{film,th}}} = (\tau - \tau_0)^{n-1} \quad (11)$$

Assuming that $n=0.5$, the term $(U_{\text{sheet}}/U_0)/(nC_{\text{film,th}})$ is plotted versus $\tau^{-0.5}$ in Fig. 14b. As seen, the numerical data are very close to the theoretical dashed line, whilst it is of interest the fact that the experimental data of Thoroddsen 2002 [61] (marked as asterisks) tend to reach the present numerical results for dimensionless time greater than 10.

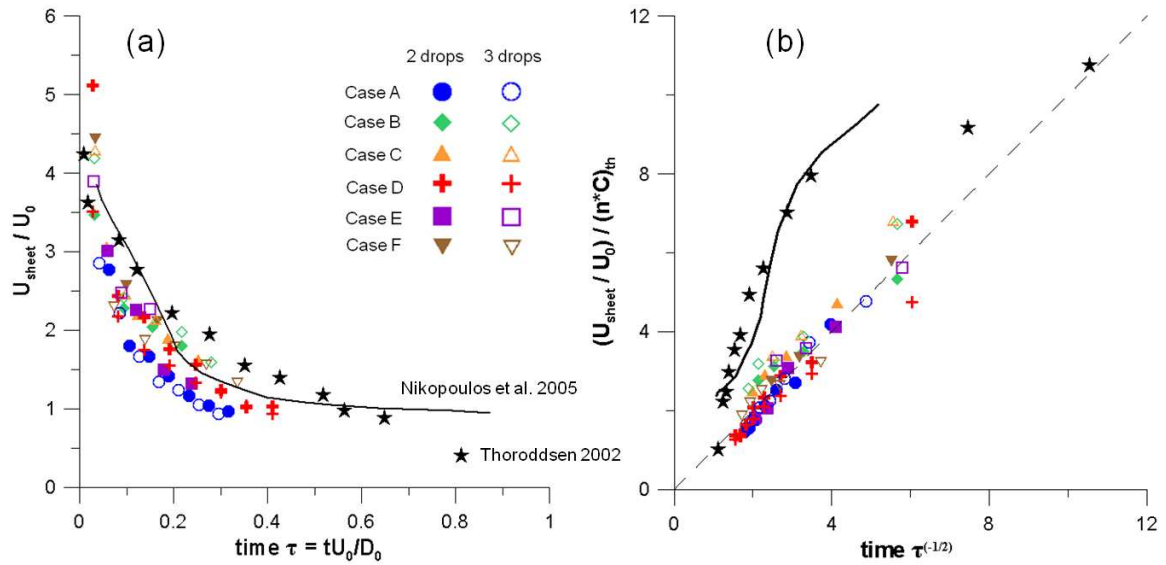


Fig. 14: In (a) dimensionless ejecta sheet velocities are plotted versus dimensionless time. In (b) the dimensionless sheet velocity is normalized with $(n \cdot C)_{\text{th}}$ and plotted versus $\tau^{-0.5}$. The

experimental data of Thoroddsen 2002 (asterisks) and the numerical predictions of Nikolopoulos et al. 2005 (solid line) for impact on a liquid film, are also shown. The dashed line in (b) represents the theoretic line.

4.7 Temporal evolution of energy terms

A powerful advantage of the numerical methods is that it is easy to extract some interesting flow features, such as the temporal evolution of the energy terms. The total energy E_{tot} of the liquid masses remains constant during the process and is composed by the kinetic energy E_{kin} , the potential energy E_{pot} , the surface energy E_{surf} and finally the energy lost due to viscous dissipation E_{diss} . These terms are calculated as:

$$E_{\text{tot},0} = E_{\text{kin}}(t) + E_{\text{pot}}(t) + E_{\text{surf}}(t) + \int_0^t \dot{E}_{\text{diss}} dt \quad (12)$$

$$E_{\text{kin}} = \sum_{\text{cells}} \left(\frac{1}{2} \rho_1 |u|^2 \text{adV} \right), \quad E_{\text{pot}} = \sum_{\text{cells}} (\rho_1 g y \text{adV}), \quad E_{\text{surf}} = \sum_{\text{cells}} (\sigma \text{dA}) \quad (13)$$

where α is the VOF value in the cell and A the surface area occupied by liquid in a cell, calculated as $A_{\text{cell}} = |\nabla \alpha| V_{\text{cell}}$. The rate at which the energy is dissipated is given by:

$$\dot{E}_{\text{diss}} = \sum_{\text{cells}} \mu \Phi V_{\text{cell}}, \quad \Phi = 2 \left[\left(\frac{\partial v}{\partial y} \right)^2 + \left(\frac{v}{y} \right)^2 + \left(\frac{\partial u}{\partial x} \right)^2 \right] + \left(\frac{\partial v}{\partial x} + \frac{\partial u}{\partial y} \right)^2 - \frac{2}{3} (\text{div} \bar{u})^2 \quad (14)$$

where Φ is the dissipation function for a two-dimensional axisymmetric case (Bird et al. (2002) [62]). The above mentioned energy terms (kinetic, potential and surface) are presented in a non-dimensional form over the initial total energy in Fig. 15a for the case A2, which is a typical case. As seen, the potential energy is negligible, whilst the kinetic energy is decreasing continuously. The surface energy increases with time, since the surface area of the liquid phase increases. The rate of viscous dissipation is presented for the cases A2, C2 and D2 in Fig. 15b,c, covering a We number range between 161 and 376 and a Re number range between 6816 and 10425. In Fig. 15b the viscous dissipation rate is non-dimensionalised with the initial kinetic energy $E_{\text{kin},0}$ divided

with the timescale D_0/U_0 reflecting the portion of the initial kinetic energy lost by viscous effects. In Fig. 15c the dissipation rate is non-dimensionalised with a reference dissipation rate scaled as $E_{\text{diss,ref}} = \mu_{\text{liq}} (U_0/D_0)^2 (\pi D_0^3/6) = \mu_{\text{liq}} U_0^2 D_0 \pi/6$. From Fig. 15b,c it is concluded that at the initial stages of impact the viscous losses are relatively high due to the impact of a moving droplet onto a stationary one, thus inducing high shear stresses. At subsequent times, they decrease and after a small period of time they increase again. This behavior is consistent with the fact that initially the base of the liquid mass in contact with the solid surface starts to expand and the velocity gradients near the solid wall, promote the energy dissipation.

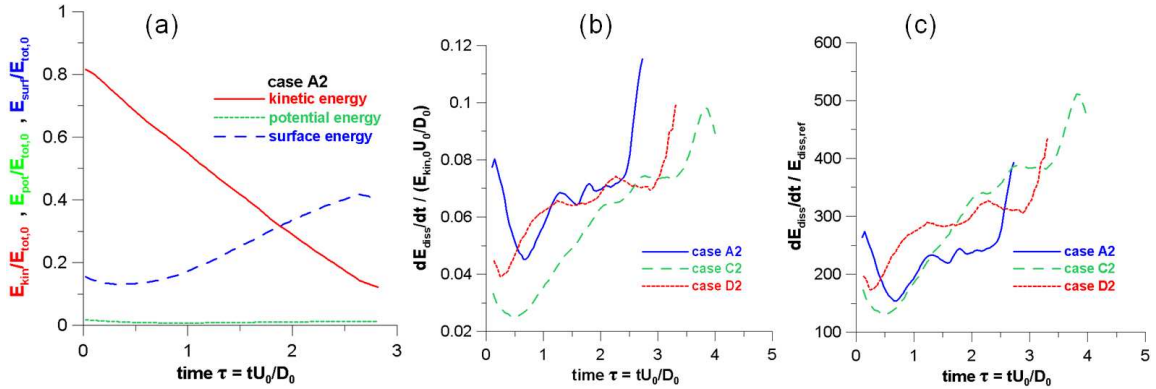


Fig. 15: Temporal evolution of the non-dimensional energy terms for the case A2 (a). In (b), (c) the dimensionless viscous dissipation for the cases A2, C2 and D2 is presented. The non-dimensionalisation of (b) represents the portion of kinetic energy lost, while in (c) viscous losses are non-dimensionalised with a reference viscous loss.

It is of interest to know where the most of the energy is lost. In Fig. 16 selected frames of case C2 showing the distribution of the viscous losses are presented. Viscous losses per unit volume are non-dimensionalised with the same way as the curves of Fig. 15b and also divided with the initial volume of the falling droplet. The reason for selecting to present the volumetric viscous losses (and not the actual) is that they are independent of the grid resolution. As seen from Fig. 16, viscous losses are maximized at the early stages of impact at the vicinity in which the two

droplets collide and at later stages at the solid-liquid interface in which strong velocity gradients are induced. The values of the dimensionless viscous losses presented in Fig. 16 have a rather qualitative character and someone should focus on their relative magnitude.

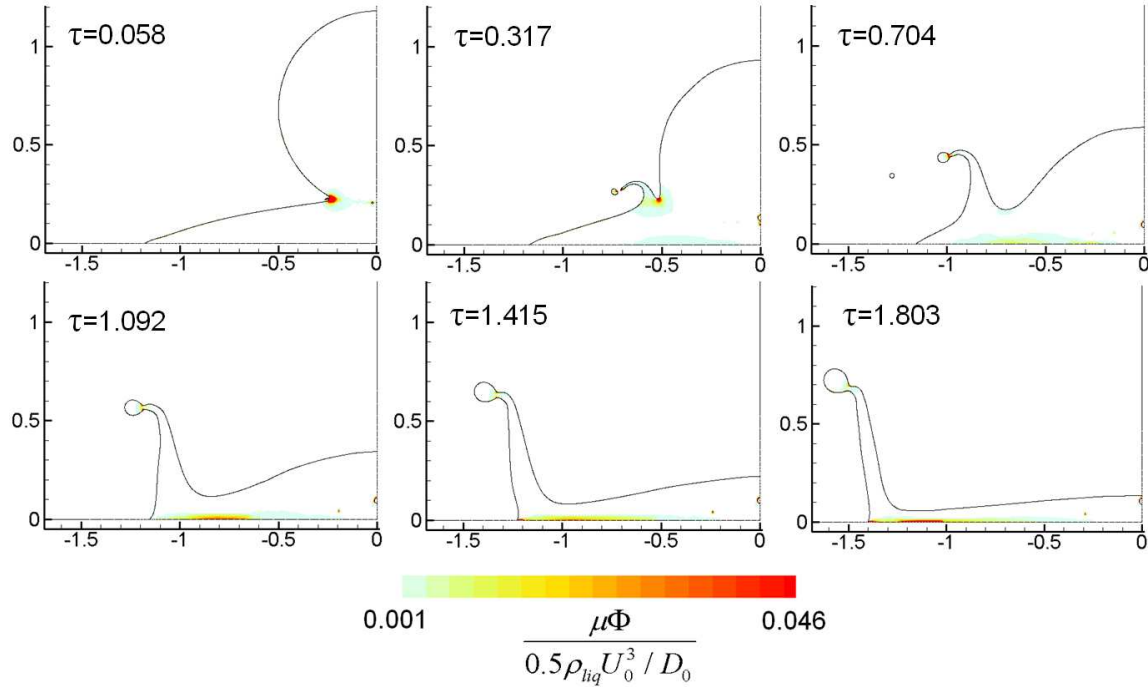


Fig. 16: Selected frames of case C2 showing the distribution of dimensionless viscous losses in each cell.

5 Conclusions

The VOF methodology has been used to predict a set of experimental data presented in detail in the first part of this work. The phenomenon of droplet impact onto a sessile droplet was approached following an axisymmetric formulation of the governing equations, which is valid for

the initial and intermediate stages of the evolution of the phenomenon, applying simultaneously an adaptive local refined unstructured grid. The predictions of the numerical model were in good agreement with the experimental data for the crown's dimensions and base diameter. Following the model validation a comprehensive discussion of the flow field regimes was presented. During the early stages of impact high pressure is built up at the points of impact and inside the liquid mass an oblique pressure gradient is developed, promoting the formation of the advancing crown. The initial pressure built-up is responsible for the entrapment of gas bubbles inside the liquid, whilst bubble rings were also identified. During the early stages of impact an ejecta sheet is formed propagating with high velocities in a radial outward direction and the measured velocities were found to be close to theoretical ones. At later stages, three-dimensional phenomena, such as the disintegration of crown's rim into secondary droplets is predicted to be occurring following the theory of Wu (2003) [60], but this cannot be represented by the adopted axisymmetric formulation.

6 Nomenclature

Symbol	Quantity	SI Unit
C, n	coefficients	-
D	diameter	m
d_c	torus diameter	m
d_{se}	torus section diameter	m
f_σ^1	surface tension force	N
h	initial sessile droplet's thickness	m
H	rim's height	m

p	pressure	N/m^2
R	radius	m
r_a	relative initial perturbation	-
$\overset{\overset{\text{I}}{\text{T}}}{\text{T}}$	stress tensor	N/m^2
t	time	s
U_0	impact velocity	m/s
u, v	velocity components	m/s
x, y	coordinates	m
V	volume	m^3
w	wettability ratio $h/D_{\text{LB},0}$	-

Greek Symbols

Symbol	Quantity	SI Unit
α	liquid volume fraction in cell	-
δ	dimensionless drop thickness h/D_0	-
κ	curvature	m^{-1}
μ	viscosity	kg/ms
ρ	density	kg/m^3
σ	surface tension coefficient	N/m
τ	non-dimensional time $\tau = tU_0 / D_0$	-

Φ dissipation function s^{-2}

subscripts

Symbol	Quantity
Q_0	Q initial
Q_{cell}	Q in cell
Q_{cr}	Q critical
Q_{equiv}	Q equivalent
Q_{exp}	Q experimental
$Q_{\text{film,th}}$	Q theoretic for impact onto a liquid film
Q_{g}	Q in gas phase
Q_{l}	Q in liquid phase
Q_{LB}	Q of the base of the lamella
Q_{LR}	Q of the rim of the lamella
Q_{tor}	Q of torus

overscripts

Symbol	Quantity
\dot{Q}	rate of Q in time
Q^*	Q dimensionless

Non-dimensional numbers

Symbol

Bo Bond number $Bo = \frac{\rho_l g D_0^2}{\sigma}$

Re Reynolds number $Re = \frac{\rho_l D_0 U_0}{\mu_l}$

Oh Ohnesorge number $Oh = \frac{\mu_l}{\sqrt{\rho_l \sigma D_0}}$

We Weber number $We = \frac{\rho_l U_0^2 D_0}{\sigma}$

Fr_h Froude number $Fr_h = \frac{U_0^2}{gh}$

abbreviations

VOF Volume Of Fluid

7 References

[1] Nikolopoulos N., Strotos G., Nikas K.S., Gavaises M., Theodorakakos A., Marengo M., Cossali G.E., Experimental investigation of a single droplet impact onto a sessile drop, Atomization and Sprays, (under review).

- [2] Rein M., Phenomena of liquid drop impact on solid and liquid surfaces, *Fluid Dynamics Research*, 12 (1993) 61-93.
- [3] Chandra S., Avedisian C.T., On the Collision of a Droplet with a Solid-Surface, *Proceedings of the Royal Society of London Series a-Mathematical Physical and Engineering Sciences*, 432 (1991) 13-41.
- [4] Roisman I.V., Rioboo R., Tropea C., Normal impact of a liquid drop on a dry surface: model for spreading and receding, *Proc. R. Soc. Lond. A* 458 (2002) 1411-1430.
- [5] Park H., Carr W., Zhu J., Morris J., Single Drop Impaction on a Solid Surface, *AIChE J.*, 49 (2003) 2461-2471.
- [6] Hatta N., Fujimoto H., Takuda H., Deformation process of a water droplet impinging on a solid surface, *Journal of Fluids Engineering, Transactions of the ASME*, 117 (1995) 394-401.
- [7] Fujimoto H., Hatta N., Deformation and rebounding processes of a water droplet impinging on a flat surface above leidenfrost temperature, *Journal of Fluids Engineering-Transactions of the ASME*, 118 (1996) 142-149.
- [8] Zhao Z., Poulikakos D., Fukai J., Heat transfer and fluid dynamics during the collision of a liquid droplet on a substrate .1. Modeling, *International Journal of Heat and Mass Transfer*, 39 (1996) 2771-2789.
- [9] Fukai J., Shiiba Y., Miyatake O., Theoretical study of droplet impingement on a solid surface below the Leidenfrost temperature, *International Journal of Heat and Mass Transfer*, 40 (1997) 2490-2492.
- [10] Waldvogel J.M., Poulikakos D., Solidification phenomena in picoliter size solder droplet deposition on a composite substrate, *International Journal of Heat and Mass Transfer*, 40 (1997) 295-309.
- [11] Butty V., Poulikakos D., Giannakouros J., Three-dimensional presolidification heat transfer and fluid dynamics in molten microdroplet deposition, *International Journal of Heat and Fluid Flow*, 23 (2002) 232-241.
- [12] Bhardwaj R., Longtin J.P., Attinger D., A numerical investigation on the influence of liquid properties and interfacial heat transfer during microdroplet deposition onto a glass substrate, *International Journal of Heat and Mass Transfer*, 50 (2007) 2912-2923.
- [13] Bhardwaj R., Attinger D., Non-isothermal wetting during impact of millimeter-size water drop on a flat substrate: Numerical investigation and comparison with high-speed visualization experiments, *International Journal of Heat and Fluid Flow*, 29 (2008) 1422-1435.

- [14] Francois M., Shyy W., Computations of drop dynamics with the immersed boundary method, Part 1: Numerical algorithm and buoyancy-induced effect, *Numerical Heat Transfer, Part B: Fundamentals*, 44 (2003) 101-118.
- [15] Francois M., Shyy W., Computations of drop dynamics with the immersed boundary method, Part 2: Drop impact and heat transfer, *Numerical Heat Transfer, Part B: Fundamentals*, 44 (2003) 119-143.
- [16] Ge Y., Fan L.S., 3-D Direct Numerical Simulation of Gas-Liquid and Gas-Liquid-Solid Flow Systems Using the Level-Set and Immersed-Boundary Methods, in: *Advances in Chemical Engineering*, 2006, pp. 1-63.
- [17] Hirt C.W., Nichols B.D., Volume of Fluid (Vof) Method for the Dynamics of Free Boundaries, *Journal of Computational Physics*, 39 (1981) 201-225.
- [18] Trapaga G., Szekely J., Mathematical modeling of the isothermal impingement of liquid droplets in spraying processes, *Metallurgical transactions. B, Process metallurgy*, 22 (1991) 901-914.
- [19] Liu H., Lavernia E.J., Rangel R.H., Numerical simulation of substrate impact and freezing of droplets in plasma spray processes, *Journal of Physics D: Applied Physics*, 26 (1993) 1900-1908.
- [20] Pasandideh-Fard M., Bhole R., Chandra S., Mostaghimi J., Deposition of tin droplets on a steel plate: simulations and experiments, *International Journal of Heat and Mass Transfer*, 41 (1998) 2929-2945.
- [21] Bussmann M., Mostaghimi J., Chandra S., On a three-dimensional volume tracking model of droplet impact, *Physics of Fluids*, 11 (1999) 1406-1417.
- [22] Pasandideh-Fard M., Aziz S.D., Chandra S., Mostaghimi J., Cooling effectiveness of a water drop impinging on a hot surface, *International Journal of Heat and Fluid Flow*, 22 (2001) 201-210.
- [23] Harvie D.J.E., Fletcher D.F., A hydrodynamic and thermodynamic simulation of droplet impacts on hot surfaces, Part I: theoretical model, *International Journal of Heat and Mass Transfer*, 44 (2001) 2633-2642.
- [24] Harvie D.J.E., Fletcher D.F., A hydrodynamic and thermodynamic simulation of droplet impacts on hot surfaces, Part II: validation and applications, *International Journal of Heat and Mass Transfer*, 44 (2001) 2643-2659.
- [25] Oguz H.N., Prosperetti A., Surface-tension effects in the contact of liquid surfaces, *J. Fluid Mech.*, 203 (1989) 149-171.

- [26] Oguz H.N., Prosperetti A., Bubble entrainment by the impact of drops on liquid surfaces, *J. Fluid Mech.*, 219 (1990) 143-179.
- [27] Yarin A.L., Weiss D.A., Impact of drops on solid surfaces: self-similar capillary waves, and splashing as a new type of kinematic discontinuity, *J. Fluid Mech.*, 283 (1995) 141-173.
- [28] Weiss D.A., Yarin A.L., Single drop impact onto liquid films: neck distortion, jetting, tiny bubble entrainment, and crown formation, *J. Fluid Mech.*, 385 (1999) 229 - 254.
- [29] Trujillo M.F., Lee C.F., Modeling crown formation due to the splashing of a droplet, *Physics of Fluids*, 13 (2001) 2503-2516.
- [30] Roisman I.V., Tropea C., Impact of a drop onto a wetted wall: description of crown formation and propagation, *J. Fluid Mech.*, 472 (2002) 373-397.
- [31] Rieber M., Frohn A., A numerical study on the mechanism of splashing, *International Journal of Heat and Fluid Flow*, 20 (1999) 455-461.
- [32] Morton D., Rudman M., Jong-Leng L., An investigation of the flow regimes resulting from splashing drops, *Physics of Fluids*, 12 (2000) 747-763.
- [33] Josserand C., Zaleski S., Droplet splashing on a thin liquid film, *Physics of Fluids*, 15 (2003) 1650-1657.
- [34] Xie H., Koshizuka S., Oka Y., Modelling of a single drop impact onto liquid film using particle method, *International Journal for Numerical Methods in Fluids*, 45 (2004) 1009-1023.
- [35] Mukherjee S., Abraham J., Crown behavior in drop impact on wet walls, *Physics of Fluids*, 19 (2007) 052103-052110.
- [36] Fujimoto H., Ogino T., Takuda H., Hatta N., Collision of a droplet with a hemispherical static droplet on a solid, *International Journal of Multiphase Flow*, 27 (2001) 1227-1245.
- [37] Fujimoto H., Ogino T., Hatta N., Takuda H., Numerical simulation of successive collision of two liquid droplets with a solid wall, *ISIJ International*, 41 (2001) 454-459.
- [38] Fujimoto H., Ito S., Takezaki I., Experimental study of successive collision of two water droplets with a solid, *Experiments in Fluids*, 33 (2002) 500-502.
- [39] Fujimoto H., Takezaki I., Shiotani Y., Tong A.Y., Takuda H., Collision dynamics of two droplets impinging successively onto a hot solid, *ISIJ International*, 44 (2004) 1049-1056.
- [40] Karl A., Frohn A., Experimental investigation of interaction processes between droplets and hot walls, *Physics of Fluids*, 12 (2000) 785-796.
- [41] Tong A.Y., Kasliwal S., Fujimoto H., On the Successive Impingement of Droplets Onto a Substrate, *Numerical Heat Transfer, Part A: Applications*, 52 (2007) 531 - 548.

- [42] Fujimoto H., Tong A.Y., Takuda H., Interaction phenomena of two water droplets successively impacting onto a solid surface, *International Journal of Thermal Sciences*, 47 (2008) 229-236.
- [43] Fluid_Research_Company, Manual on the GFS CFD code, in, 2002 , www.fluid-research.com.
- [44] Nikolopoulos N., Theodorakakos A., Bergeles G., Normal impingement of a droplet onto a wall film: a numerical investigation, *International Journal of Heat and Fluid Flow*, 26 (2005) 119-132.
- [45] Nikolopoulos N., Theodorakakos A., Bergeles G., Three-dimensional numerical investigation of a droplet impinging normally onto a wall film, *Journal of Computational Physics*, 225 (2007) 322-341.
- [46] Nikolopoulos N., Nikas K.-S., Bergeles G., A numerical investigation of central binary collision of droplets, *Computers & Fluids*, 38 (2009) 1191-1202.
- [47] Nikolopoulos N., Theodorakakos A., Bergeles G., Off-centre binary collision of droplets: A numerical investigation, *International Journal of Heat and Mass Transfer*, 52 (2009) 4160-4174.
- [48] Strotos G., Nikolopoulos N., Nikas K.-S., A parametric numerical study of the head-on collision behavior of droplets, *Atomization and Sprays*, 20 (2010) 191-209.
- [49] Nikolopoulos N., Theodorakakos A., Bergeles G., A numerical investigation of the evaporation process of a liquid droplet impinging onto a hot substrate, *International Journal of Heat and Mass Transfer*, 50 (2007) 303-319.
- [50] Strotos G., Gavaises M., Theodorakakos A., Bergeles G., Numerical investigation on the evaporation of droplets depositing on heated surfaces at low Weber numbers, *International Journal of Heat and Mass Transfer*, 51 (2008) 1516-1529.
- [51] Strotos G., Gavaises M., Theodorakakos A., Bergeles G., Numerical investigation of the cooling effectiveness of a droplet impinging on a heated surface, *International Journal of Heat and Mass Transfer*, 51 (2008) 4728-4742.
- [52] Strotos G., Gavaises M., Theodorakakos A., Bergeles G., Evaporation of a suspended multicomponent droplet under convective conditions, in: *ICHMT, Marrakech, Morocco, 2008*.
- [53] Strotos G., Gavaises M., Theodorakakos A., Bergeles G., Influence of species concentration on the evaporation of suspended multicomponent droplets, in: *ILASS 2008, Como Lake, Italy, 2008*.

- [54] Theodorakakos A., Bergeles G., Simulation of sharp gas-liquid interface using VOF method and adaptive grid local refinement around the interface, *International Journal for Numerical Methods in Fluids*, 45 (2004) 421-439.
- [55] Brackbill J.U., Kothe D.B., Zemach C., A continuum method for modeling surface tension, *Journal of Computational Physics*, 100 (1992) 335-354.
- [56] Jasak H., Error analysis and estimation for finite volume method with applications to fluid flows, in, Ph.D Thesis, Imperial College of Science Technology & Medicine, University of London, 1996.
- [57] Ubbink O., Issa R.I., A method for capturing sharp fluid interfaces on arbitrary meshes, *Journal of Computational Physics*, 153 (1999) 26-50.
- [58] Ubbink O., Numerical prediction of two fluid systems with sharp interfaces, in, PhD Thesis, Department of Mechanical Engineering, Imperial College of Science, Technology & Medicine, University of London, 1997.
- [59] Thoroddsen S.T., Etoh T.G., Takehara K., Air entrapment under an impacting drop, *J. Fluid Mech.*, 478 (2003) 125-134.
- [60] Wu Z.N., Approximate critical Weber number for the breakup of an expanding torus, *Acta Mechanica*, 166 (2003) 231-239.
- [61] Thoroddsen S.T., The ejecta sheet generated by the impact of a drop, *J. Fluid Mech.*, 451 (2002) 373-381.
- [62] Bird R.B., Stewart W.E., Lightfoot E.N., *Transport Phenomena*, 2nd ed., Wiley, New York, 2002.